PAPER

Check for updates

In situ K$_2$S activated electrospun carbon nanofibers with hierarchical meso/microporous structures for supercapacitors†

Hua Liu, [ID] *[a] Weiguo Song [ID] [b] and Aihua Xing*[a]

Porous electrospun carbon nanofibers (CNFs) can be produced by a more advantageous '*in situ* activation' method by electrospinning polyacrylonitrile (PAN) with an activation agent. However, most *in situ* activated electrospinning processes yield porous CNFs with rather limited surface area and less porosity due to the inappropriately selected activation agents. Here we found K$_2$S could perfectly meet both compatibility and reactivity requirements of PAN electrospinning to generate hierarchical meso/micropores inside electrospun CNFs. During the whole fabrication process, K$_2$S experiences a phase evolution loop and the hierarchical pore structures are formed by the reaction between K$_2$S oxidative derivatives and the as-formed carbon during heat treatment. The hierarchical meso/microporous CNFs not only showed a large surface area (835.0 m^2 g^{-1}) but also exhibited a high PAN carbonization yield (84.0 wt%) due to improved cyclization of PAN's nitrile group during the pre-oxidation stage. As an electrode material for supercapacitors, the corresponding electrodes have a capacitance of 210.7 F g^{-1} at the current density of 0.2 A g^{-1} with excellent cycling durability. The hierarchically porous CNFs produced *via in situ* activation by K$_2$S combine the advantages of interconnected meso/micropores and are a promising candidate for electrochemical energy conversion and storage devices.

1. Introduction

Electrochemical double-layer capacitors (EDLCs) store charge and release energy based on the formation of oppositely charged layers at the interface of the electrolyte and electrodes.[1–6] The reversible fast-surface-charge-storage process of ions between an electrolyte and high accessible surface area electrodes (*e.g.*, carbon, transition metal oxides or hydroxides and conducting polymers) endows supercapacitors with high power density and long cycling lifetime that are widely employed as electric energy storage devices. Up until now, supercapacitors have still been plagued by their insufficient energy density, hindering their scope of applications, especially when a high-energy output is required.[7] One of the critical issues is the implementation of ideal electrode materials, which require a high conductivity, large ion-accessible specific surface area (SSA) and appropriate pore size distribution,[8–12] because the electric double-layer formation is determined by surface chemistry and apertures of pores upon carbon materials.[13–16]

The electrode materials need to possess both high specific surface area and appropriate pore size distribution that combines narrow micropores suitable for ion accommodation with mesopores favorable for ion transport.

Electrospun PAN based carbon nanofibers can offer large surface area accessible to the electrolyte, efficient electron and ion transport, and structural stability to prevent the electrode from destruction due to swelling and shrinkage, which is very crucial to real application in supercapacitors.[7] Carbon nanofibers with hierarchical meso/microporous structure are highly desirable for the improved performance of supercapacitors.[17–23] While micropores provide a large accessible surface area for ion charge accommodation, mesopores could offer low-resistant channels for fast ion transportation. However, conventional electrospinning technique can only produce solid carbon nanofibers, and the resultant electrospun CNFs possess nonporous structure with very low SSA of 10–30 m^2 g^{-1} which greatly hindered the utilization of electrospun CNFs as electrode materials in supercapacitors. Great efforts have been made to enrich the pore structure of electrospun CNFs to improve the reversible fast-surface-charge-storage process of ions between an electrolyte and high accessible surface area electrodes in EDLCs. Pore generating methods such as utilizing sacrificial agents (PMMA,[24–26] PTA,[27] SiO$_2$ nanoparticles,[28] *etc.*) and post activation by steam,[29–32] KOH[33,34] and CO$_2$,[35–37] had been utilized to produce porous electrospun CNFs. However, most of these methods suffered from disadvantages of

[a]National Institute of Clean-and-Low-Carbon Energy, Beijing 102211, P. R. China. E-mail: hua.liu.w@chnenergy.com.cn; aihua.xing@chnenergy.com.cn

[b]Beijing National Laboratory for Molecular Sciences (BNLMS), Key Laboratory of Molecular Nanostructure and Nanotechnology, Institute of Chemistry, Chinese Academy of Sciences, Beijing, 100190, P. R. China

complicated manufacturing process with high temperature, high cost, or environmental destructiveness, and more than half of carbon precursor mass of sacrificial polymer agents are consumed to develop porous structure during the activation process resulting in high price, significantly limiting their further application in most supercapacitors.

Porous electrospun CNFs can also be produced in a simpler manner that enables the formation of porous structure under the presence of an additional activated phase in PAN/dimethylformamide (DMF) electrospinning solution during heat treatment processes. The porous structured carbon nanofibers were formed due to *in situ* catalytic behaviors of the second activated phase in the carbon nanofibers, such as organic compound ($Fe(acac)_2$,[38] nano-$CaCO_3$,[39,40] *etc*) and inorganic compounds ($ZnCl_2$,[41] $CoCl_2$,[42] $Co(NO_3)_2$ $6H_2O$,[43] *etc*). Unfortunately, using the above activation agents generally yield porous carbon nanofibers with rather limited surface area and less porosity (less than 550 m^2 g^{-1} and 0.4 cm^3 g^{-1}) and the as-prepared porous CNFs contain large amount of doped metal which have to be removed by acid rinsing. All of these unfavorable aspects could be mainly ascribed to the inappropriately selected activation agents. Hence, one has to find a more effective activation agent in the electrospinning solution system for the fabrication of porous CNFs with high SSA and porosity.

There are two key requirements for a second phase activation agent for the successful synthesis of PAN-based porous CNFs: (1) the compatibility and electrospinnability of an activation agent in PAN/DMF solution; (2) the reactivity between activation agent and the as-formed carbon nanofibers. In this study, we found for the first time that K_2S could perfectly meet both requirements to generate hierarchical meso/micropores inside electrospun CNFs. 1D carbon nanofibers composed of hierarchical meso- and microporous structures were produced by electrospinning PAN and K_2S followed by thermal treatment and water washing. During the electrospinning and preoxidative processes, K_2S transformed into its oxidative derivatives (*e.g.* polysulfide, thiosulfate, pyrosulfate and sulfate state) which served as real activation species reacting with the as-formed carbon nanofibers to generate porous structure. The sample not only show a large SSA (835.0 m^2 g^{-1}), but also exhibited a high PAN carbonization yield of (84.0 wt%) which is due to improved cyclization of nitrile group during the pre-oxidation stage with the addition of K_2S. The sample combines the advantages of interconnected meso- and micropores and has shown excellent performance as an electrode material for supercapacitors.

2. Experimental

2.1 Fabrication of PAN–K_2S composite nanofibers

A common electrospinning method was used to fabricate the composite precursor nanofibers. In a typical procedure, calculated amount of K_2S was dissolved in 10 g of DMF (Alfa) by magnetic stirring for 30 min, followed by adding 1.0 g of PAN (150 000, Aldrich) into the above solution at 80 °C and stirring for 2 h to form a homogeneous suspension, all steps are operated in N_2 atmosphere to prevent K_2S from oxidizing to K_2S_2

under the air. The violet suspension was transferred into a plastic syringe equipped with a 17 gauge stainless needle which was connected to a high-voltage supply. The distance from the needle to the grounded aluminium foil was set at 15 cm and the voltage was adjusted at 25 kV with solution feeding rate of 1.5 mL h^{-1}. The as-prepared pale yellow PAN–K_2S composite nanofibers were peeled off from the aluminium foil collector and was denoted as As_PAN_*x*, where *x*% indicates the content of K_2S in the electrospun PAN–K_2S nanofiber sample.

2.2 Preparation of porous carbon nanofiber

The nonwoven mat was put into a horizontal tube furnace and was heated to 280 °C in air (2 °C min^{-1}) with subsequent pre-oxidative stabilization for 2 h. For carbonization and *in situ* activation, the sample was heated up to 800–1000 °C (4 °C min^{-1}) and kept for 2 h under argon gas flow (60 mL min^{-1}). After cooling under Ar atmosphere, the porous carbon nanofibers were obtained by washing with deionized water three times followed by drying at 120 °C for 8 h. The pre-oxidative sample were denoted as Pre_PAN_*x* and the obtained carbon nanofibers were designated as Car[*y*]_CNF_*x*, where *x*% represent the weight percentage of K_2S in the electrospun PAN–K_2S nanofiber sample and *y* stands for carbonization temperature.

2.3 Characterization

The electrospinning solution parameters were determined by using AR-2000 rheometer and Accumet Excel XL50 for viscosity and conductivity measurements, respectively. Surface tensions of solutions were measured using interfacial tensiometer (CSC-Denouy 70545). The structures and morphologies of the products were characterized by transmission electron microscope (TEM, JEOL-1011) and scanning electron microscope (SEM, JEOL 6701F). The nitrogen adsorption and desorption isotherms were collected on Quantachrome Autosorb AS-1 Instrument. The X-ray diffraction (XRD) patterns of samples were recorded on Bruker X-ray diffractometer using Cu Kα radiation (40 kV, 40 mA). Raman spectra were measured using LabRam HR-800 micro-Raman spectroscopy system.

Thermal behavior of pre-oxidation fibers were studied using a differential scanning calorimeter (NETZSCH STA449F3) with a heating rate of 10 °C min^{-1} under air in the range of 30–360 °C. Thermal decomposition behavior were investigated by thermo-gravimetric and differential thermal analysis (TG/DTA 6300), which were performed between ambient and 1000 °C with heating rate of 10 °C min^{-1} under flowing air. The mass carbonization yield of CNFs was calculated based on corresponding TG curves according to eqn (1):

$$R = 1 - \frac{W(250°C) - W(400°C)}{W(250°C) \times (1-r)} \times 100\% \qquad (1)$$

where R is carbonization mass yield; W(250 °C) and W(400 °C) are sample weight determined from TG curves under the temperature in the bracket; r is the calculated mass content of as-formed K_2SO_4 in K_2S/PAN composite nanofibers.

Infrared spectra were recorded on Bruker VERTEX in attenuated total reflectance (ATR) mode. The spectra were collected at room temperature in the scanning range of 650–4000 cm^{-1} (2 cm^{-1} resolution) using Hg–Cd–Te (MCT) detector with averaging 64 scans. The X-ray photoelectron spectroscopy (XPS, ESCALAB 250Xi) was used to evaluate the elemental compositions. The binding energy scales were calibrated in reference to the C 1s peak position (284.6 eV).

2.4 Electrochemical measurements

Two pieces of porous CNF electrodes with a separator was assembled in to a symmetrical two-electrode coin to evaluate the capacitive performance in an KOH aqueous system (electrolyte: 6 M KOH). Both the electrode materials and separator were previously immersed in 6 M KOH solution under vacuum for 24 h to achieve sufficient electrolyte saturation before assembly. Cyclic voltammogram (CV) measurement (scanning rates varying from 5 to 200 mV s^{-1}) was conducted on an electrochemistry workstation (Princeton PARSTAT 2273). Galvanostatic charge/discharge (GCD) measurements were conducted with a charge–discharge tester (Arbin 2000) with current density varying from 0.2 to 20 A g^{-1}. Electrochemical impedance spectroscopy (EIS) measurements were recorded on Princeton PARSTAT 2273 in the frequency region of 100 kHz to 0.1 Hz. A three-electrode system were also employed for the measurements, with a 1 cm × 1 cm Pt sheet and SCE (saturated calomel electrode) as counter and reference electrodes respectively. The working electrode was assembled by pressing the carbon nanofiber mat and nickel foam (used as the current collector) together without any additional binders or conductive additives.

3. Results and discussion

K$_2$S can be easily dissolved in DMF (Fig. S1†) and it has shown an excellent compatibility with PAN, ensuring a homogeneous dark green solution without any phase separation in DMF solution. Besides, K$_2$S possesses high melting point (m. p. 840 °C) and high boiling point (b. p. 912 °C) and can undergo reaction with air to form various oxidative states to react with the as-formed carbon. All of the above properties of K$_2$S allowed us to anticipate that K$_2$S would be an interesting *in situ* activation agent for the fabrication of porous carbon nanofibers. Verification experiments of this assumption mainly consisted of three steps to prepare K$_2$S activated carbon nanofibers: (1) electrospinning of K$_2$S–PAN composite nanofibers; (2) preoxidative stabilization of K$_2$S–PAN composite nanofibers in air at 280 °C; (3) carbonization of electrospun K$_2$S–PAN composite nanofibers and *in situ* activation under high temperature.

Fig. 1a shows the N$_2$ adsorption/desorption isotherms of as-prepared carbon nanofibers with 0 wt%, 10.0 wt%, 20.0 wt%, and 30.0 wt% addition of K$_2$S in the K$_2$S–PAN composite nanofibers, and remarkable difference was observed among these samples. The as-prepared carbon nanofiber with the K$_2$S addition above 20 wt% possesses massive adsorption capacity in low relative pressure (P/P_0 < 0.05) and a hysteresis loop (type
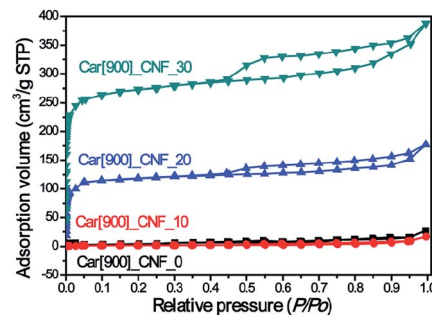

Fig. 1 N$_2$ adsorption/desorption isotherms of as-prepared carbon nanofibers under 900 °C.

H4) at a relative pressure range of 0.45–0.95, indicating that the as-formed carbon nanofibers features both massive micropores and mesopores inside the carbon nanofibers. On the other hand, for carbon nanofiber prepared with the K$_2$S addition below 10 wt%, neither adsorption in low relative pressure nor hysteresis loop at high relative pressure was observed, indicating nonporous structure inside the carbon nanofibers. This had confirmed our assumption that K$_2$S was surely an excellent activation agent for the fabrication of porous carbon nanofiber. Table 1 further illustrates the detailed difference of pore structures among these samples. The total surface area of sample Car[900]_CNF_30 reached up to 835.0 m^2 g^{-1} with 78.5% of microporous surface area (655.5 m^2 g^{-1}) and the micropore volume (0.387 cm^3 g^{-1}) occupied 57.1% of the total pore volume (0.678 cm^3 g^{-1}) (Table 1). Sample Car[900]_CNF_20 with less addition of K$_2$S exhibited much less total surface area (325.6 cm^3 g^{-1}) and pore volume (0.314 cm^3 g^{-1}) than Car[900]_CNF_30. For carbon nanofiber with K$_2$S less than 10 wt%, the total surface area of Car[900]_CNF_10 and Car[900]_CNF_0 were only 7.0 and 10.0 m^2 g^{-1} respectively, indicating no micro/mesoporous structures were formed, which suggested that a threshold amount of K$_2$S was required to generate meso-/microporous structure during the activation process.

The morphologies of electrospun PAN and K$_2$S/PAN composite nanofibers with different K$_2$S contents were recorded by using SEM method. As shown in Fig. 2, all the samples exhibit continuous and long 1D nanofiber interconnecting to form 3D nonwoven membrane under the same electrospun conditions. While the diameter of pure PAN nanofiber was 382.1 nm, all K$_2$S/PAN composite nanofibers demonstrate lower fiber diameter with 214.9 nm, 200.5 nm and 250.3 nm for As_PAN_10, As_PAN_20 and As_PAN_30, respectively. This is due to that the diameter of electrospun nanofiber is governed by a complex set of parameters of electrospinning solution, including viscosity, surface tension and electrical conductivity.[42] The decreased diameter of K$_2$S/PAN composite nanofibers with the addition of K$_2$S is mainly due to the enhanced conductivity of the electrospun solution (Table 2), which facilitate concentration of charge on the tip surface and help overcoming the surface tension under electrostatic force.[44] Further increasing K$_2$S addition did not follow this rule as we didn't observe an decreasing fiber diameter with continuing to

Table 1 Pore structure of as-prepared porous carbon nanofibers determined by N_2 adsorption/desorption isotherms at 77 K

Sample	K_2S content (wt%)	S_{BET} (m² g⁻¹)	S_{meso} (m² g⁻¹)	S_{micro} (m² g⁻¹)	V_{total} (cm³ g⁻¹)	V_{meso} (cm³ g⁻¹)	V_{micro} (cm³ g⁻¹)	d_{HK} (nm)	d_{BJH} (nm)
Car[900]_CNF_0	0	10.0	—	—	0.032	—	—	—	—
Car[900]_CNF_10	10	7.0	—	—	0.021	—	—	—	—
Car[900]_CNF_20	20	325.6	123.2	201.4	0.314	0.104	0.210	0.557	3.90
Car[900]_CNF_30	30	835.0	316.2	518.8	0.618	0.234	0.387	0.563	3.81
Car[800]_CNF_30	30	655.2	320.9	334.3	0.486	0.238	0.248	0.541	3.97
Car[1000]_CNF_30	30	614.8	282.7	332.1	0.435	0.200	0.235	0.601	4.06

increase K_2S content, probably due to K_2S interacting with PAN that cause the increased viscosity of the electrospun solution (Table 2). After carbonization, the fiber diameter of all samples further shrunk to half of its original diameter due to the removal of volatile species during thermal treatment. Instead of nonporous structure in the neat CNFs, all K_2S activated CNFs exhibit porous structure insides fiber matrix (Fig. S2†).

Fig. 2 SEM images and diameter distribution of as-prepared electrospun K_2S/PAN composite nanofibers with different K_2S contents: (a and b) 0 wt% (pure PAN nanofibers), (c and d) 10 wt%, (e and f) 20 wt% and (g and h) 30 wt%. Scale bar denotes 5 μm.

As PAN nanofibers converted to carbon nanofibers, oxidative stabilization is considered to be the most decisive step for developing dimensional stability during thermal treatment, since it significantly governs the desired structure with an infusible stable ladder polymer structure that do not melt at high temperature processing and avoid excessive volatilization of elemental carbonaceous material in carbonization step.[45] In order to determine the influence of K_2S on the oxidative stabilization process, we performed TG/DTG and DSC on electrospun K_2S/PAN composite nanofibers in air. As shown in Fig. 3a, all As_PAN samples experienced two different periods of transformation: oxidative stabilization at *ca.* 300 °C and consumption of carbon in air at temperature above 500 °C. Pure PAN nanofibers exhibited a strong DTG peak (Fig. S3†) corresponding to complex and multiple chemical reactions (*e.g.*, cracking, dehydration, cyclization, dehydrogenation, crosslinking).[40,41,46] Two important reactions, *i.e.* dehydrogenation and cyclization reaction, occur during this period under the oxidative atmosphere. Since cyclization of nitrile groups to form this stable ladder polymer structure does not involve weight loss, the weight loss during oxidative process is mainly due to the C–C dissociation of PAN forming low molecular weight volatile.[47] The lower bond energy for the C–C dissociation of PAN was reported at 297 kJ mol⁻¹ in the main PAN chain, corresponding to 330 °C for 30 min half weight loss temperature.[48] With increasing K_2S content in the as-prepared K_2S/PAN composite nanofibers, the DTG peak shifted to higher temperature and declined rapidly with a broadening peak wing (Fig. S3†). When the K_2S concentration exceeded 10 wt%, the DTG peak diminished completely. Some residual remained above 800 °C in the case of the K_2S/PAN nanofiber samples owing to the presence of K_2S, while for pure PAN nanofiber sample, nanofibers were completely decomposed. It is noteworthy that the carbonization yield of carbon nanofiber is greatly improved with the increased K_2S content determined from eqn (1), suggesting that K_2S might catalyze the oxidative stabilization process, promoting the cyclization reaction and decreasing the cracking reaction. DSC curves of K_2S/PAN composite nanofibers containing different K_2S contents were recorded at temperatures ranging from 50 to 350 °C to confirm this presumption. As shown in Fig. 3b, all four nanofiber samples exhibit a relatively large and sharp exothermic peak centered at *ca.* 180 to 300 °C. Pure electrospun PAN nanofibers demonstrates a strong exothermic peak centered at *ca.* 294 °C,
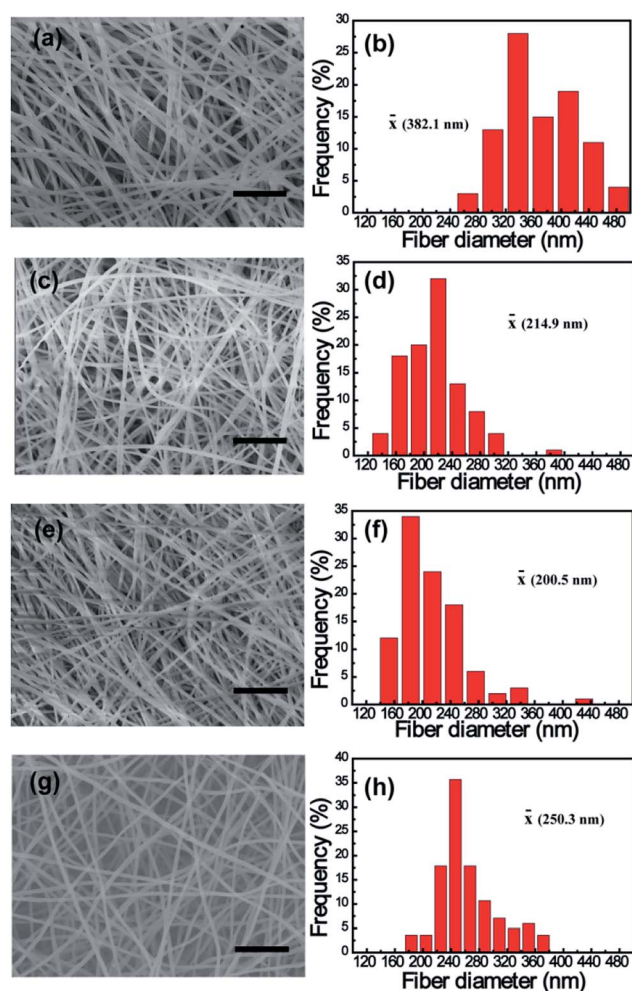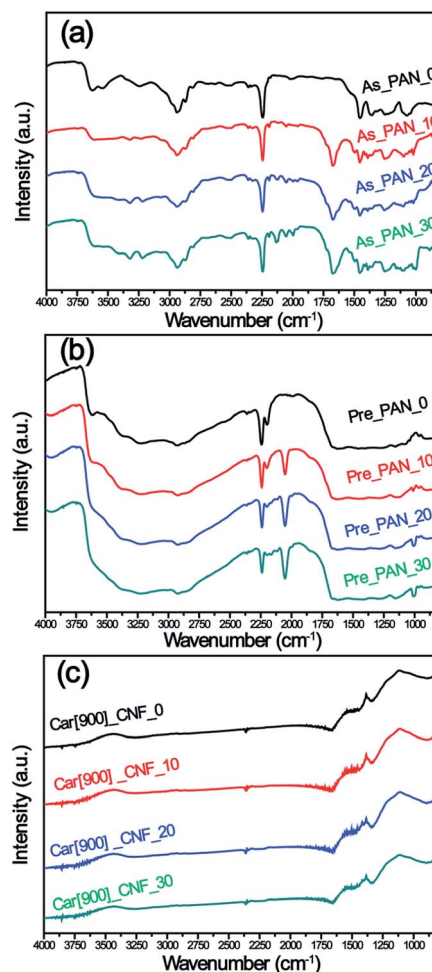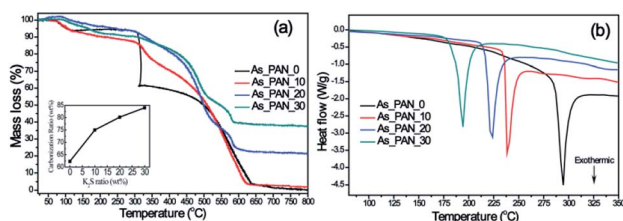
Table 2 Characteristics of measured electrospinning solution parameters and diameters of electrospun K_2S/PAN composite nanofibers

K_2S content (wt%)	Viscosity (Pa s)	Surface tension (mN m^{-1})	Conductivity (μs cm)	K_2S/PAN diameter (nm)	CNF diameter (nm)
0	0.82	34.7	53.0	382.1 ± 50.3	187.0 ± 19.1
10	0.88	35.1	325.1	214.9 ± 30.7	120.5 ± 20.6
20	0.91	34.4	846.7	200.5 ± 28.8	137.9 ± 17.3
30	1.05	35.0	1643.5	250.3 ± 25.1	122.2 ± 10.3

while the presence of K_2S in the nanofibers significantly lowers this exothermic peak (ca. 238 °C), and further increasing K_2S content (20 wt% and 30 wt%) results in continuous lower exothermic temperatures of 223 and 194 °C respectively. The DCS results indicate that K_2S acted as a catalyst to promote the cyclization of nitrile group during the pre-oxidation stage, causing this lower cyclization temperature compared with that of pure PAN nanofibers. More stable ladder polymer structure are formed under the oxidative process with the increase of K_2S addition, and this will significantly alleviate the C–C dissociation of PAN main chain from causing poor quality of carbon nanofibers. Therefore, the yield of carbonization rises and less weight loss occurred during the oxidative stabilization process with the increasing addition of K_2S.

ATR-FTIR for all samples was recorded to understand the effect of K_2S on the structure change of PAN during different stages (Fig. 4). For the as-prepared K_2S/PAN nanofibers (Fig. 4a), the peak at 2240 cm^{-1} in the infrared spectra was assigned to the –C≡N stretching of the acrylonitrile unit in the polymer chains, and the peak at 2940 cm^{-1} and 2870 cm^{-1} correspond to the asymmetric and symmetric stretching of –CH$_2$– groups respectively.[49] 1453 cm^{-1} can be ascribed to bending –CH$_2$ and 1360 cm^{-1} correspond to CH bending and –CH$_2$ wagging adsorption. Upon addition of K_2S, a new adsorption peak at 1673 cm^{-1} emerged, which can be ascribed to C=N stretching, indicating that K_2S or its oxidative compounds can react with the cyan groups of PAN to form C=N group. The small stretching vibration peaks of C≡N at the range of 2170–1943 cm^{-1} corresponds to inorganic C≡N groups formed with addition of K_2S. Upon exposure to oxidative atmosphere during the preoxidative stage (Fig. 4b), –C≡N stretching (2240 cm^{-1}) of the acrylonitrile was largely preserved along with the appearance of a new conjugated –C≡N (2200 cm^{-1}) group, and both of which gradually decreased with increasing addition of K_2S.

Another sharp vibration adsorption peak at 2050 cm^{-1} emerged with addition of K_2S during this stage, and this peak can be ascribed to –C≡N stretching of –S–C≡N group, indicating that K_2S or its derivatives reacted with cyan group of PAN to form –S–C≡N group. After carbonization process (Fig. 4c), all samples without water washing exhibit similar IR pattern, and all C≡N and –S–C≡N stretching vibration disappeared. Small peaks with similar intensity were still observable at 1673 cm^{-1} indicating that C=N group were still preserved in the carbon nanofiber matrix.
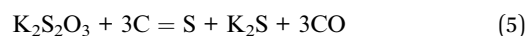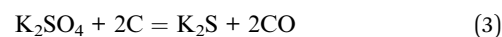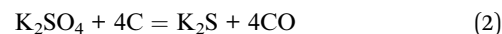

Fig. 3 (a) TGA thermograms and the calculated carbonization ratio curve (inset), (b) DSC curves of as-prepared K_2S/PAN composite nanofibers with different K_2S contents.

Fig. 4 ATR-FTIR spectra of (a) K_2S/PAN composite nanofibers, (b) preoxidative K_2S/PAN composite nanofibers and (c) carbon nanofibers with different K_2S contents.

To better understand the activation mechanism of K_2S during the formation of porous CNFs, XRD were recorded to detect the phase evolution of K_2S and PAN throughout the whole processes. As can be seen in Fig. 5a, freshly prepared PAN nanofibers feature two typical diffraction peaks at $2\theta = 16.5°$ and $2\theta = 29.0°$ which correspond to the crystal plane (100) reflecting the spacing of molecular chain and (110) crystal plane of the nearly parallel molecular pieces.[50] Upon addition of K_2S into PAN matrix, the substantially decreased characteristic diffraction peaks of PAN suggested that the addition of K_2S significantly influenced the long-range order of PAN matrix resulting in this disordered orientation and decreased crystallinity of PAN matrix. As for the phase transformation of K_2S, situation became much more complex as the unstable K_2S under oxidative environment transformed into its oxidative derivatives with more than one phase, which included oxidative sulfide mixtures of KS, K_2S_3, K_2S_4 and K_2S_5, sulfur, and sulfate mixtures of K_2SO_3, K_2SO_5, K_2SO_7, and K_2SO_4, *etc.* From Fig. 5a, we could identify that the oxidative extent of K_2S is determined by the amount of K_2S added within PAN matrix, the sulfide mixtures constitutes high content with more K_2S addition in K_2S/PAN composite nanofiber.

Fig. 5b depicts the XRD patterns of K_2S/PAN composite nanofibers treated in air. Upon experiencing preoxidation where cyclization reaction typically occurs, all K_2S/PAN composite nanofiber shows a drastic decrease of the diffraction peak at 16.9° compared to PAN nanofibers, which is due to the improved cyclization reaction with the help of K_2S. Meanwhile, K_2S in Pre_PAN samples transformed into its sulfate form during the oxidative stabilization process. As for sample Pre_PAN_10 with 10 wt% K_2S, the diffraction peaks match well with standard diffraction peaks of K_2SO_4 (JCPDF 25-0681) suggesting that K_2S was fully oxidized into its highest oxidation state during the pre-oxidative stage. When the K_2S content was increased to 20 wt%, the diffraction peaks of the transformed K_2S in sample Pre_PAN_20 could be attributed to compounds of sulfate and thiosulfate form. For the carbonization process at

900 °C, all the four CNF samples exhibited similar diffraction pattern assigned to the (002) and (101) diffraction of hexagonal carbon material (JCPDS card No. 75-1621),[51] indicating the crystalline nature of carbon with very small particle size.[52] It is worth noted that all K_2S-related compound diffraction peaks disappeared among all the samples, this is probably because the as-formed thiosulfate and sulfate compounds reacted with carbon under the reducing atmosphere to form the terminal K_2S compounds which could be easily escape from carbon nanofiber under the temperature near its boiling point (912 °C, K_2S). The structural perfections of carbon nanofibers were investigate by Raman spectroscopy in Fig. 5d. All samples possess identical intensity ratios ($R = I_D/I_G$), indicating that the perfectness of structurally ordered graphite phases in the carbon nanofibers was not affected by the addition of K_2S.

From the above results, we could conclude that it was the mixtures of potassium thiosulfate, potassium sulfate and potassium pyrosulfate that were reacting with the as-formed carbon nanofiber resulting in such porous structure in carbon nanofiber. The possible K_2S evolution during the whole process and the activation mechanism is proposed as follows:

$$K_2SO_4 + 4C = K_2S + 4CO \tag{2}$$

$$K_2SO_4 + 2C = K_2S + 2CO \tag{3}$$

$$K_2S_2O_7 + 4C = SO_3 + K_2S + 4CO \tag{4}$$

$$K_2S_2O_3 + 3C = S + K_2S + 3CO \tag{5}$$

During the electrospinning process, K_2S within the PAN matrix transformed into as-formed polysulfide and thiosulfate state, and these newly generated mixtures were further transformed into deeper oxidation state (*e.g.* pyrosulfate and sulfate) during the preoxidative process. Under the carbonization process, the as-formed potassium sulfate, potassium pyrosulfate and potassium thiosulfate consumed the as-formed carbon in the CNF matrix forming porous structure according to the proposed eqn (2)–(5), and this process also accompanied with the formation of the terminal product of K_2S at the end of this activation process. When the carbonization temperature rises above the boiling point of K_2S, the formed K_2S escapes out of the CNF matrix (Scheme 1) leaving only porous structures in the CNF matrix.

800 °C, 900 °C and 1000 °C were chosen to investigate the effect of carbonization temperature on the pore structure of micro/mesoporous carbon nanofibers based on the fact that the
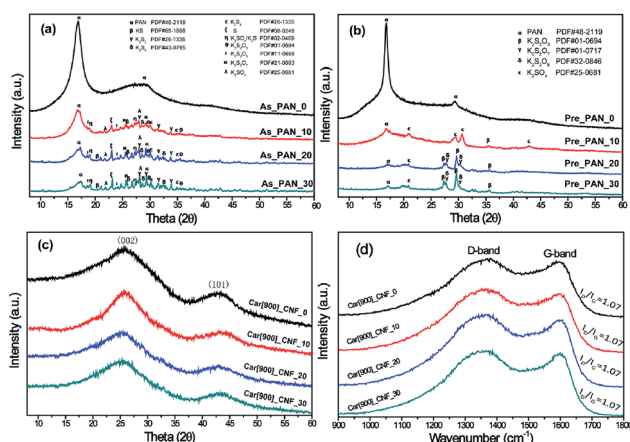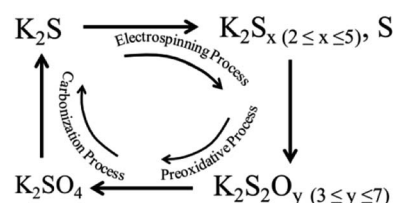

Fig. 5 XRD patterns of (a) as prepared K_2S/PAN samples, (b) preoxidative K_2S/PAN samples, (c) as-prepared carbon nanofibers prepared at 900 °C without wash and (d) the corresponding Raman spectra.

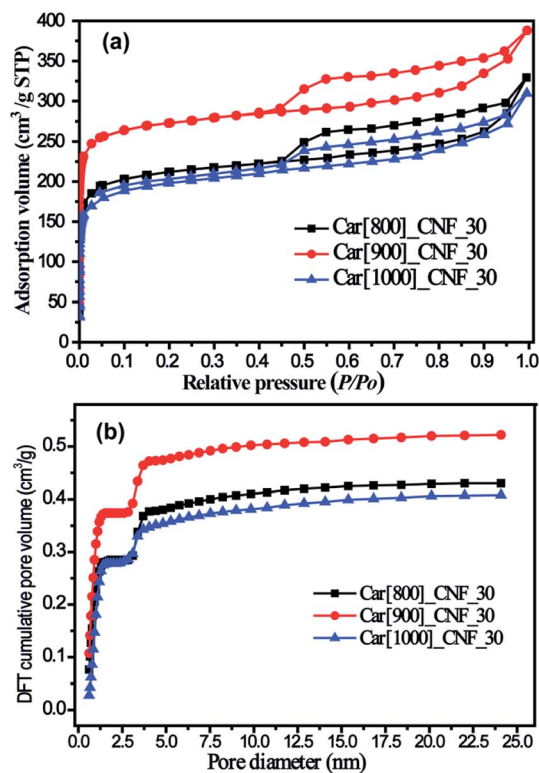**Scheme 1** Schematic diagram of the K_2S evolution during the whole processes.

Fig. 6 (a) N_2 adsorption/desorption isotherms of as-prepared carbon nanofibers under various temperature and (b) corresponding DFT cumulative pore volume curves.

melting point (840 °C) and boiling point (912 °C) of K_2S were in the range of 800–1000 °C. N_2 adsorption/desorption isotherms of as-prepared porous carbon nanofibers with the 30% K_2S addition were shown in Fig. 6. All three samples exhibit similar hysteresis loop (type H4) at a relative pressure range of 0.45–0.95, indicating that these three samples possesses similar porous structure with the mesopore volume being 0.238 cm³ g⁻¹ for Car[800]_CNF_30, 0.234 cm³ g⁻¹ for Car[900]_CNF_30 and 0.200 cm³ g⁻¹ for Car[1000]_CNF_30, respectively (Table 1). Significant different adsorption capacities in low relative pressure ($P/P_0 < 0.05$) were observed among these three samples. Carbonization of K_2S/PAN composite nanofibers at 900 °C yielded the most abundant microporosity with 0.387 cm³ g⁻¹ of micropore volume and 518.8 m² g⁻¹ of microporous surface area for Car[900]_CNF_30. Whereas for carbonization

temperature at 800 °C and 1000 °C, only 0.248 cm³ g⁻¹ and 0.235 cm³ g⁻¹ of micropore volume were observed for Car[800]_CNF_30 and Car[1000]_CNF_30 respectively, which is much less than that of Car[900]_CNF_30 (Table 1). This is probably because K_2S was at a molten state under the temperature of 900 °C and can improve the activation with the local as-formed carbon nanofiber more efficiently than that under 800 °C, thus generating more pores inside carbon nanofibers. When the carbonization temperature reached 1000 °C, which is beyond the boiling point of K_2S, part of K_2S will evaporate from the local carbon nanofiber and will thus inevitably lower the effectiveness of activation. Therefore, carbonization temperature of 900 °C would be optimum activation temperature for the synthesis of porous CNFs.

Surface functionalization is important for the electrochemical performance of carbon electrode materials. Table 3 shows the composition of all as-prepared carbon nanofiber samples. The overall C and N contents of K_2S activated carbon nanofibers are a little lower than that of neat CNFs (Car[900]_CNF_0) suggesting that the cyan group can be abstracted from the PAN matrix with the help of K_2S, which is in accordance with FT-IR results (Fig. 4b). The overall oxygen contents are enhanced from 9.48% to 12–14 wt% for K_2S activated carbon nanofibers due to oxidation by K_2S oxidative derivates. Note the sample were thoroughly washed with DI water prior to XPS characterization, no sulfur and potassium signals were determined indicating all sulfur and potassium can be removed simply by water washing. N 1s spectrum of carbon nanofiber samples could be fitted into three component peaks at 396.6 eV, 397.4 eV, and 399.2 eV (Fig. 7), corresponding to three types of nitrogen functional groups, *i.e.* N-6 (pyridinic N), N-5 (pyrrolic N), and N-Q (quaternary N), respectively.[13,53–56] For carbon nanofiber samples obtained at 900 °C, all samples exhibited three types of nitrogen with different relative amounts. Upon increasing K_2S contents, the intensity of N-Q gradually decreases and its proportion is becoming smaller, while both N-5 and N-6 are increasing in terms of intensity and proportion. These results indicate that the activation agent tends to induce nitrogen atom of PAN into formation of polypyrrole (pentagonal ring, N-5) and polypyridinic (six-membered ring, N-6) structure rather than the formation of N-Q during carbonization process. It is also reported that among these three types of commonly observed N-doped atoms, N-6 and N-5 could offer more active sites to enhance the pseudocapacitance, resulting in improved the power density of supercapacitors.[54,57,58] Hence, it is

Table 3 Results of C 1s, N 1s, and O 1s core level XPS spectra of Car[900]_CNF samples

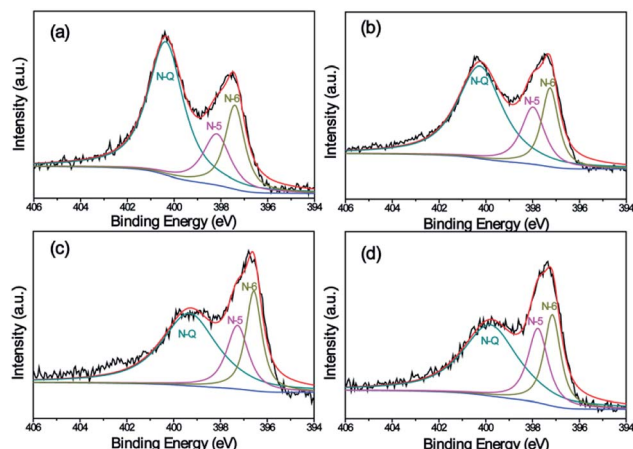| Sample	C 1s (at%)	O 1s (at%)	N 1s (at%)	Nitrogen functional groups (at%)	
				N-Q	N-5 + N-6
Car[900]_CNF_0	84.04	9.48	6.46	3.94	2.50
Car[900]_CNF_10	81.46	13.41	5.13	3.11	2.02
Car[900]_CNF_20	81.01	13.71	5.26	3.00	2.26
Car[900]_CNF_30	81.68	12.59	5.71	3.22	2.49

Fig. 7 High-resolution XPS spectra of the N 1s peak of samples: (a) Car[900]_CNF_0, (b) Car[900]_CNF_10, Car[900]_CNF_20, and (d) Car[900]_CNF_30.

reasonable to believe that Car[900]_CNF_30 of high amount of N-5 and N-6 structures, combined with high surface area and porosity, possess the necessity for high capacitive performance of supercapacitors.

The supercapacitive performance of the samples as electrode materials were evaluated based on a two-electrode configuration in a liquid electrolyte of 6 M KOH at room temperature. Fig. 8a shows the comparative CV plots at a scan rate of 5 mV s^{-1} of all samples with different K$_2$S mass addition. The areas surrounded by the CV curves of Car[900]_CNF_30 and Car[900]_CNF_20 are much larger than that of Car[900]_CNF_10 and Car[900]_CNF_0, indicative of much higher specific capacitance for carbon nanofiber electrode prepared with K$_2$S addition exceeding 20 wt%. Car[900]_CNF_30, which possess the highest surface area of 835.0 m^2 g^{-1}, has the highest specific capacitance (Cs) of 217.8 F g^{-1}. Fig. 8b shows the CV measurement results of Car[900]_CNF_30 at different scanning rates from 5 to 200 mV s^{-1}. Notwithstanding the pseudo-rectangular shape of CV curves on the two-electrode configuration (Fig. 8a and b) which is usually taken for pure capacitive behavior, the CV curve of Car[900]_CNF_30 in three-electrode system shows evidently distorted CV profile (Fig. S4a†), especially at negative potentials, indicating pseudocapacitive contribution due to the side reactions in charge and discharge process by the appreciable contents of O and N groups. The corresponding calculated specific capacitances in the three-electrode system determined from CV curves are shown in Fig. S4b,† which presents a similar situation as in the two-electrode system.

Fig. 8c shows the GCD curves of CNFs samples with an applied current density of 0.2 A g^{-1}, the highest specific capacitance of 210.7 F g^{-1} was also obtained by using Car[900]_CNF_30 and the Cs sequence among all samples was in accordance with the results of the cyclic voltammetry. The GCD curves at different current densities are shown in Fig. 8d and f. The typical GCD profiles of Car[900]_CNF_30 demonstrate highly symmetry and relatively linear indicating ideal capacitive behavior. When the current density raised up to 20 A g^{-1}, the

specific capacitance stays at 83% of the highest Cs value, reflecting the high rate capability of Car[900]_CNF_30. The specific capacitances of all samples against the scanning rate calculated by CV curves are displayed in Fig. 8e. The Cs values clearly show that an increase of scanning rate from 5 to 200 mV s^{-1} decreases the capacitance value, which is commonly happened on carbon materials and caused by the short time available for ion diffusion and adsorption inside micropores.[59] Car[900]_CNF_30 demonstrated high Cs retention capability (70% of the highest Cs) at high scanning rate of 200 mV s^{-1}, indicating high power handling capability due to the open pore structure (inter-fiber spacing) in nanofiber mats resulting in faster electrolyte/ion diffusion. As for the electrochemical stability in charge/discharge cycles for supercapacitors, 89% of the initial capacitance is retained after 10 000 cycles in the electrochemical stability test equipped with the Car[900]_CNF_30 at a current density of 20 A g^{-1} (Fig. 8g).
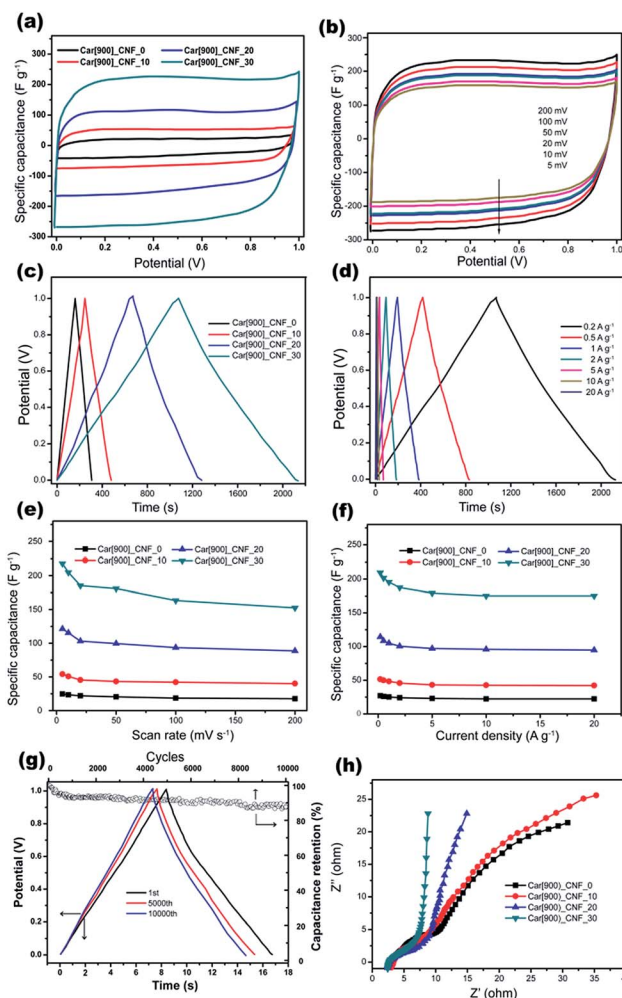

Fig. 8 Electrochemical properties of carbon nanofiber samples in a two-electrode system of 6 M KOH solution. CV curves for (a) all samples and (b) different scanning rates with Car[900]_CNF_30, GCD curves for (c) all samples and (d) different current density with Car[900]_CNF_30, specific capacitance of all samples calculated from (e) CV curves and (f) GCD methods, (g) cycling stability of Car[900]_CNF_30 and (h) Nyquist plots of all samples.

The Nyquist plots of different samples were compared in Fig. 8h. At high frequencies, a semi-circular arc is related to intrinsic resistance of active material and the contact resistance between working electrode and electrolyte.[60,61] The smaller diameter of semicircle in the EIS spectrum of Car[900]_CNF_30 indicates lower resistance which is associated with better electrolyte pore accessibility.[41] In the low frequency region, Car[900]_CNF_30 demonstrates the most steep line suggesting more ideal capacitive behavior. Calculated from the GCD curve at a current density of 1 A g^{-1} (Fig. 8d), Car[900]_CNF_30 delivered a high energy density of 27.2 W h kg^{-1} with a power density of 508.7 W kg^{-1}, and the energy density is 24.3 W h kg^{-1} even at the high power density of 10.4 kW kg^{-1} indicating high energy storage capability under high current density. Compared with those published on electrospun carbon fibers and activated carbons (Table S1†), the performance of Car[900]_CNF_30 is competitive among the electrode carbons reported, and this further demonstrates that the formation of hierarchical porous structures could effectively improve the power density of the device.

As it has been proposed that energy storage of electric double layer is mainly dependent on electrode/electrolyte interface performance, it is crucial for the electrode materials to have suitable pore size, reasonable proportion of micropores, high surface area and surface functionalities which can improve the EDL and pseudocapacitance. The superior capacitive performance of Car[900]_CNF_30 can be due to the nanofibrous structure that offers excellent accessibility for electrolyte ions, and the hierarchical porosity (0.618 cm^3 g^{-1}) with rational ratio of micropores to mesopores (3 : 2) and high SSA (835.0 m^2 g^{-1}) induced by the activation of K_2S during carbonization stage, which facilitate the accessibility of electrolyte ions to the interior surface of the porous carbon resulting in improved formation of electric double layer. Therefore, porous electrospun carbon nanofibers prepared *via* K_2S *in situ* activation could be promising candidates for supercapacitors.

4. Conclusions

In summary, for the first time we found K_2S is a perfect activation agent for the successful fabrication of hierarchical porous CNFs with high SSA and porosity by employing *in situ* activation electrospinning method. During the whole fabrication process, K_2S experiences a phase evolution loop including oxidation and reduction process. The former process involves the transformation of K_2S to its oxidative derivatives and the improved cyclization of PAN nitrile groups during the electrospinning and preoxidative stages, the latter includes the K_2S oxidative derivatives transforming back to K_2S accompanied with the activation of CNFs during carbonization stage. The as-prepared hierarchical porous CNFs not only show a large SSA (835.0 m^2 g^{-1}), but also exhibited a high PAN carbonization yield of (84.0 wt%). The hierarchical porous CNFs combine the advantages of interconnected meso/micropores and are a promising candidate for electrochemical energy conversion and storage devices.

Conflicts of interest

There are no conflicts to declare.

Acknowledgements

References

1 Z. Wu, L. Li, J. M. Yan and X. B. Zhang, *Adv. Sci.*, 2017, **4**, 1600382.

2 P. Simon and Y. Gogotsi, *Acc. Chem. Res.*, 2013, **46**, 1094–1103.

3 E. Frackowiak, K. Metenier, V. Bertagna and F. Beguin, *Appl. Phys. Lett.*, 2000, **77**, 2421–2423.

4 S. Li, C. Zhao, K. W. Shu, C. Y. Wang, Z. P. Guo, G. G. Wallace and H. K. Liu, *Carbon*, 2014, **79**, 554–562.

5 G. Lota, K. Fic and E. Frackowiak, *Electrochem. Commun.*, 2011, **13**, 38–41.

6 S. T. Senthilkumar, R. K. Selvan, Y. S. Lee and J. S. Melo, *J. Mater. Chem. B*, 2013, **1**, 1086–1095.

7 J. J. Xue, T. Wu, Y. Q. Dai and Y. N. Xia, *Chem. Rev.*, 2019, **119**, 5298–5415.

8 R. Hou, G. S. Gund, K. Qi, P. Nakhanivej, H. Liu, F. Li, B. Y. Xia and H. S. Park, *Energy Storage Materials*, 2019, **19**, 212–241.

9 Y. M. Tan, C. F. Xu, G. X. Chen, Z. H. Liu, M. Ma, Q. J. Xie, N. F. Zheng and S. Z. Yao, *ACS Appl. Mater. Interfaces*, 2013, **5**, 2241–2248.

10 B. Liu, H. Shioyama, H. L. Jiang, X. B. Zhang and Q. Xu, *Carbon*, 2010, **48**, 456–463.

11 M. Biswal, A. Banerjee, M. Deo and S. Ogale, *Energy Environ. Sci.*, 2013, **6**, 1249–1259.

12 P. Hao, Z. H. Zhao, J. Tian, H. D. Li, Y. H. Sang, G. W. Yu, H. Q. Cai, H. Liu, C. P. Wong and A. Umar, *Nanoscale*, 2014, **6**, 12120–12129.

13 L. J. Hou, Z. G. Hu, X. T. Wang, L. L. Qiang, Y. Zhou, L. W. Lv and S. S. Li, *J. Colloid Interface Sci.*, 2019, **540**, 88–96.

14 M. J. Bleda-Martinez, J. A. Macia-Agullo, D. Lozano-Castello, E. Morallon, D. Cazorla-Amoros and A. Linares-Solano, *Carbon*, 2005, **43**, 2677–2684.

15 D. Lozano-Castello, D. Cazorla-Amoros, A. Linares-Solano, S. Shiraishi, H. Kurihara and A. Oya, *Carbon*, 2003, **41**, 1765–1775.

16 Y. T. Li, L. Liu, Y. Z. Wu, T. Wu, H. Y. Wu, Q. P. Cai, Y. T. Xu, B. R. Zeng, C. H. Yuan and L. Z. Dai, *J. Mater. Chem. B*, 2019, **7**, 13154–13163.

17 T. Kim, G. Jung, S. Yoo, K. S. Suh and R. S. Ruoff, *ACS Nano*, 2013, **7**, 6899–6905.

18 S. Dutta, A. Bhaumik and K. C. W. Wu, *Energy Environ. Sci.*, 2014, **7**, 3574–3592.

19 Y. M. He, W. J. Chen, C. T. Gao, J. Y. Zhou, X. D. Li and E. Q. Xie, *Nanoscale*, 2013, **5**, 8799–8820.

20 S. J. Song, F. W. Ma, G. Wu, D. Ma, W. D. Geng and J. F. Wan, *J. Mater. Chem. B*, 2015, **3**, 18154–18162.

21 X. B. Yan, Z. X. Tai, J. T. Chen and Q. J. Xue, *Nanoscale*, 2011, **3**, 212–216.

22 L. J. Xie, G. H. Sun, F. Y. Su, X. Q. Guo, Q. Q. Kong, X. M. Li, X. H. Huang, L. Wan, W. Song, K. X. Li, C. X. Lv and C. M. Chen, *J. Mater. Chem. B*, 2016, **4**, 1637–1646.

23 Y. L. Wen, L. P. Zhang, J. Liu, X. Wen, X. C. Chen, J. L. Ma, T. Tang and E. Mijowska, *Nanotechnology*, 2019, **30**, 295703.

24 G. Li, T. S. Xie, S. L. Yang, J. H. Jin and J. M. Jiang, *J. Phys. Chem. C*, 2012, **116**, 9196–9201.

25 W. H. Li, Z. Z. Yang, Y. Jiang, Z. R. Yu, L. Gu and Y. Yu, *Carbon*, 2014, **78**, 455–462.

26 R. Zhang, L. Wang, J. Zhao and S. W. Guo, *ACS Sustainable Chem. Eng.*, 2019, **7**, 632–640.

27 H. Liu, C. Y. Cao, F. F. Wei, P. P. Huang, Y. B. Sun, L. Jiang and W. G. Song, *J. Mater. Chem. B*, 2014, **2**, 3557–3562.

28 L. W. Ji, Z. Lin, A. J. Medford and X. W. Zhang, *Carbon*, 2009, **47**, 3346–3354.

29 Z. Y. Guo, J. T. Huang, Z. H. Xue and X. M. Wang, *Chem. Eng. J.*, 2016, **306**, 99–106.

30 S. Y. Kim and B. H. Kim, *J. Power Sources*, 2016, **328**, 219–227.

31 D. Nan, Z. H. Huang, F. Y. Kang and W. C. Shen, *New Carbon Materials*, 2016, **31**, 393–398.

32 M. X. Wang, Z. H. Huang, T. Shimohara, F. Y. Kang and K. M. Liang, *Chem. Eng. J.*, 2011, **170**, 505–511.

33 C. Ma, Y. Song, J. L. Shi, D. Q. Zhang, X. L. Zhai, M. Zhong, Q. G. Guo and L. Liu, *Carbon*, 2013, **51**, 290–300.

34 C. Ma, R. R. Wang, Z. Y. Xie, H. X. Zhang, Z. Y. Li and J. L. Shi, *J. Porous Mater.*, 2017, **24**, 1437–1445.

35 Q. Dong, G. Wang, B. Q. Qian, C. Hu, Y. W. Wang and J. S. Qiu, *Electrochim. Acta*, 2014, **137**, 388–394.

36 C. H. Kim, J. H. Wee, Y. A. Kim, K. S. Yang and C. M. Yang, *J. Mater. Chem. B*, 2016, **4**, 4763–4770.

37 S. Zhang, Q. Zhang, H. Y. Wang, Y. H. Ni and Z. B. Zhu, *Int. J. Hydrogen Energy*, 2014, **39**, 17913–17920.

38 J. S. Cho, J. S. Park and Y. C. Kang, *Nano Res.*, 2017, **10**, 897–907.

39 L. J. Zhang, Y. Z. Jiang, L. W. Wang, C. Zhang and S. X. Liu, *Electrochim. Acta*, 2016, **196**, 189–196.

40 H. Liu, C.-Y. Cao, F.-F. Wei, Y. Jiang, Y.-B. Sun, P.-P. Huang and W.-G. Song, *J. Phys. Chem. C*, 2013, **117**, 21426–21432.

41 C. Kim, B. T. N. Ngoc, K. S. Yang, M. Kojima, Y. A. Kim, Y. J. Kim, M. Endo and S. C. Yang, *Adv. Mater.*, 2007, **19**, 2341–2346.

42 Y. Aykut, *ACS Appl. Mater. Interfaces*, 2012, **4**, 3405–3415.

43 Y. Liu, J. Y. Zhou, L. L. Chen, P. Zhang, W. B. Fu, H. Zhao, Y. F. Ma, X. J. Pan, Z. X. Zhang, W. H. Han and E. Q. Xie, *ACS Appl. Mater. Interfaces*, 2015, **7**, 23515–23520.

44 X. H. Qin, E. L. Yang, N. Li and S. Y. Wang, *J. Appl. Polym. Sci.*, 2007, **103**, 3865–3870.

45 M. S. A. Rahaman, A. F. Ismail and A. Mustafa, *Polym. Degrad. Stab.*, 2007, **92**, 1421–1432.

46 K. K. Karthikeyan and P. Biji, *Microporous Mesoporous Mater.*, 2016, **224**, 372–383.

47 Q. Ouyang, L. Cheng, H. Wang and K. Li, *Polym. Degrad. Stab.*, 2008, **93**, 1415–1421.

48 G. Henrici-Olivé and S. Olivé, *The chemistry of carbon fiber formation from polyacrylonitrile*, Berlin, Heidelberg, 1983, pp. 1–60.

49 E. Cipriani, M. Zanetti, P. Bracco, V. Brunella, M. P. Luda and L. Costa, *Polym. Degrad. Stab.*, 2016, **123**, 178–188.

50 M. M. Qiao, H. J. Kong, X. M. Ding, Z. F. Hu, L. W. Zhang, Y. Z. Cao and M. H. Yu, *Polymers*, 2019, **11**, 403.

51 F. Su, C. K. Poh, J. S. Chen, G. Xu, D. Wang, Q. Li, J. Lin and X. W. Lou, *Energy Environ. Sci.*, 2011, **4**, 717–724.

52 F. Zheng, Y. Yang and Q. Chen, *Nat. Commun.*, 2014, **5**, 5261.

53 W. Lei, L. L. Han, C. J. Xuan, R. Q. Lin, H. F. Liu, H. L. L. Xin and D. L. Wang, *Electrochim. Acta*, 2016, **210**, 130–137.

54 R. Singhal and V. Kalra, *J. Mater. Chem. B*, 2015, **3**, 377–385.

55 J. Tan, Y. L. Han, L. He, Y. X. Dong, X. Xu, D. N. Liu, H. W. Yan, Q. Yu, C. Y. Huang and L. Q. Mai, *J. Mater. Chem. B*, 2017, **5**, 23620–23627.

56 T. Le, Y. Yang, Z. H. Huang and F. Y. Kang, *J. Power Sources*, 2015, **278**, 683–692.

57 W. R. Li, D. H. Chen, Z. Li, Y. F. Shi, Y. Wan, J. J. Huang, J. J. Yang, D. Y. Zhao and Z. Y. Jiang, *Electrochem. Commun.*, 2007, **9**, 569–573.

58 U. B. Nasini, V. G. Bairi, S. K. Ramasahayam, S. E. Bourdo, T. Viswanathan and A. U. Shaikh, *J. Power Sources*, 2014, **250**, 257–265.

59 T. Le, Y. Yang, Z. Huang and F. Kang, *J. Power Sources*, 2015, **278**, 683–692.

60 A. Garcia-Gomez, P. Miles, T. A. Centeno and J. M. Rojo, *Electrochim. Acta*, 2010, **55**, 8539–8544.

61 C. Portet, P. L. Taberna, P. Simon and C. Laberty-Robert, *Electrochim. Acta*, 2004, **49**, 905–912.